On the Analysis and Interpretation of Turbulent Velocity Fields

R. J. ADRIAN, K. T. CHRISTENSEN, Z.–C. LIU

Laboratory for Turbulence and Complex Flow

Department of Theoretical and Applied Mechanics

University of Illinois, Urbana, IL 61801

Abstract

Methods of analyzing and interpreting velocity-field data (both two- and three-dimensional) to understand the kinematics, dynamics, and scales of turbulence are discussed. Reynolds decomposition and vorticity are traditionally used; however, several other methods, including Galilean (constant convection velocity) and LES decompositions (low-pass filtering), in conjunction with critical point analysis of the local velocity gradient tensor, reveal more about the structure of turbulence. Once the small-scale structures have been identified, it is necessary to assess their importance to the overall dynamics of the turbulence by visualizing the motions they induce and the stresses they impose both on other small-scale vortices and the larger-scale field.

1 Introduction

Over the past fifteen years of turbulence research, the amount of information obtained through the application of new experimental and computational tools has grown immensely. The two-dimensional (2-D) velocity vector fields obtained by particle image velocimetry (PIV) and the three-dimensional (3-D) fields obtained by direct numerical simulation (DNS), large eddy simulation (LES) and holographic PIV (HPIV) provide new insight into the scales, kinematics, and dynamics of turbulence and demand new methods of extracting this information and interpreting it properly. These methods *must* take advantage of the quantitative nature of the data.

Reynolds decomposition into mean and fluctuating portions is the *de facto* standard method of describing *turbulent* velocity fields. While the fluctuating fields found by Reynolds decomposition are the correct basis for the analysis of statistics, they do not always constitute the best method for visualizing the turbulent mechanics of a flow. The method that is best suited to a particular investigation is determined by the questions one asks. If the ultimate goal is to understand statistical interrelationships, so as to contribute to improved Reynolds-averaged Navier-Stokes models, then Reynolds decomposition is the correct choice. However, if one wishes to focus on the dynamics of small-scale vortices, or on the contribution of small structures to the stresses acting on larger structures, then methods that unambiguously detect small eddies may be better suited. Alternatively, if one wishes to understand the structured coherent elements of the flow, then methods of visualization that leave the large structures intact may be more appropriate.

While the foregoing considerations seem quite apparent, the use of Reynolds decomposition is so widespread and so ingrained in the turbulence community that it is used almost universally, regardless of its suitability for a particular purpose. A primary goal of this paper is to discuss several other decomposition methods and to articulate their uses in addressing various questions about turbulence.

The issue of identifying vortices in a flow field first arose with the advent of flow visualization techniques (dye injection, smoke-wire, etc.). The patterns created by these techniques represent streaklines. Hama (1962) showed that streaklines observed in a shear flow perturbed by a traveling sinusoidal wave of constant amplitude can roll-up, falsely indicating the

presence of discrete vortices. Gursul et al. (1990) argue that it is crucial to choose the correct reference frame in which to visualize streakline patterns because a steady flow can appear unsteady in an *incorrect* frame of reference. These two examples serve to indicate that visualization of vortices using streaklines may be ambiguous. This is because streaklines represent traces of particle images over both a limited portion of the flow and a long-time interval. Velocity vector fields, on the other hand, cover the entire field and represent motion over a very short time. We shall see, however, that interpretation of velocity vector fields also requires care.

Identification of vortices in a velocity field, along with calculation of vortex statistics (i.e., size, strength, etc.), is normally accomplished by identifying isolated 'regions' of significant vorticity (vortex 'cores') (Jiménez et al. 1993). In simple flows with minimal shear, this task is relatively straightforward. However, in complex flow fields, this is not the case. Vortices are often 'masked' by regions of significant shear, making it nearly impossible to obtain reliable vortex statistics. In this case, it is extremely difficult to use vorticity maps to identify vortices and to assess their contribution to the overall flow.

This paper offers new methods for extracting information from velocity fields about the scales, kinematics, and dynamics of turbulence. These ideas are also appropriate for other complex flows in general, but the focus of this paper will be on turbulence, wherein some of the greatest challenges lie. Specifically, we wish to identify small-scale vortices and determine their contribution to the overall dynamics of the flow. Alternative methods to Reynolds averaging include decomposition by Galilean transformation and by filtered fields, as in LES. This filtering can be homogeneous (a Gaussian filter, for example) or inhomogeneous (as in proper orthogonal decomposition (POD)). These particular methods separate the field based on the scale of the fluid motions in space or time. Yet another class of decompositions is based on classifying points in the turbulent field according to a certain property (or group of properties), such as rotation. The field is then decomposed into regions based on the magnitude of that property. A classic example of this is to separate the velocity field into toroidal and poloidal fields. Modern eddy classifiers (swirling strength analysis) based on the mathematics of the local velocity gradient tensor will also be discussed and compared to vorticity.

2 Decomposition by Scale

Decomposition by scale denotes separating the total vector field into portions having different scales of length or time. For example, let $\boldsymbol{u}$ be the total velocity vector and let

$$U(x,t) \equiv \langle u \rangle \tag{1}$$

be the mean of the total velocity, defined either by ensemble averaging, time averaging or spatially averaging in a statistically homogeneous direction. The Reynolds decomposition

$$u = U + u' \tag{2}$$

can then be viewed as a scale decomposition in several ways, depending upon the definition of the mean. If the mean is determined by long-time averaging, the decomposition separates the field into a (possible position dependent) component that has infinite time-scale and a fluctuation that contains all other components of lesser time-scale. If the mean is found by averaging in one or more spatial directions, then the mean may vary both in time and in the non-averaging directions, and the decomposition separates the field into a component that has infinite scale in the averaging directions and a component that fluctuates on finite spatial scales and in time. Note that either approach is extreme because, out of the full space-time spectrum of motions, the decomposition only isolates the component that has infinite scale from all others. This is illustrated graphically in Figure 1. One can easily question the singular importance of $k = 0$ or $\omega = 0$, as opposed to isolating the components that are merely large-scale in space and/or time.

A more general approach is to define a decomposition by separating the space-time spectrum of the field into two or more groups, each representing different aspects of the field (Figure 1). Separation done purely in space is essentially the approach of LES decomposition. The large-eddy field is defined by low-pass filtering the total velocity as

$$\overline{u}(x,t) = \int_D f(x'-x)u(x',t)\,dx' \tag{3}$$

to obtain the filtered (large-scale) field, $\overline{u}$. (f is the filtering kernel and D is the domain of the velocity field) The total field is then the sum of the large-scale field and the remaining smaller-scale field

$$u = \overline{u} + u''. \tag{4}$$

This type of decomposition is extremely useful in visualizing small-scale turbulent eddies because it removes the translation imposed by the larger-scale field on the small-scale vortices. Note that the filtering kernel, f, can either be defined using a standard homogeneous filter (Gaussian, top-hat, etc.) or by proper orthogonal decomposition for inhomogeneous flows. This will be discussed in greater detail in Section 3.3.

Galilean transformation is the simplest method of decomposition, although not one that necessarily involves scale decomposition. The total velocity is represented as the sum of a constant convection velocity, $\boldsymbol{U_c}$, plus the deviation

$$\boldsymbol{u} = \boldsymbol{U}_c + \boldsymbol{u}_c . \tag{5}$$

If the convection velocity is a freely-selected constant, the Galilean transformation removes a constant that is independent of space and time, i.e. $k = \omega = 0$ (Figure 1). However, if $\boldsymbol{U_c}$ is found by averaging over a local region, then the convection velocity corresponds to a moving average, which has the properties of a low-pass filter. In PIV, the measured vector field is often averaged over the entire field of view, and this value is then subtracted from the total field before displaying it.

As mentioned earlier, the choice of decomposition method can have a dramatic effect on the visualization of the resulting fluctuating field. In the coming sections, we will consider these effects on the visualization of both small-scale vortices and the events that contribute to the turbulent (Reynolds) stresses.

3 Visualization of Vortices

It has been surprisingly challenging for the fluid dynamics community to arrive at a consensus definition of a vortex or an eddy, as evidenced by the many proposals one can find in the recent research literature (Chong et al. 1990; Dallman et al. 1991; Jeong and Hussain 1995; Zhou et al. 1996, 1999; among others). While a widely accepted definition does not currently exist, the various methods that have been proposed all arrive at broadly similar results. For the present time, it is sufficient to refer to the definition offered by Kline and Robinson (1989 a, b): "A vortex exists when instantaneous streamlines mapped onto a plane normal to the core exhibit a roughly circular or spiral pattern, when viewed in a reference frame moving with the center of the vortex core." A *key* condition in this definition is that the velocity field must be viewed in a

frame that moves at the same velocity as the core of the vortex. A second *key* condition is that the vorticity is concentrated in a "core". If a turbulent field consists of large-scale motion with many small-scale vortices embedded within it, it will only be possible to recognize a vortex in terms of the foregoing definition if the velocity at the center of each small vortex is removed. An important function of decomposition by scale is to do exactly this.

We choose to use a Galilean analysis where we cycle through a range of convection velocities in order to identify all of the structures in any given velocity field using the Kline and Robinson (1989 a, b) definition. Figure 2 illustrates the effect of convection velocity on the visualization of a turbulent eddy. Removing a velocity which is less than the translational velocity of the vortex is shown in Figure 2(a). Since the streamlines are not closed, by the definition of Kline and Robinson (1989 a, b), the vortex is not properly visualized. The true frame of reference of the vortex is shown in Figure 2(b). Finally, overestimation of the convection velocity of the vortex again results in open streamlines (Figure 2(c)). This technique is consistent with the spirit of Michalke (1964). It is also helpful, as a secondary check, to "confirm" the existence of an eddy by comparing the location of the apparent center of the closed streamlines to the maximum in the local concentration of vorticity or swirling strength (see Section 3.4).

To illustrate these ideas, we will use a typical PIV realization in the radial-streamwise plane of fully-developed turbulent pipe flow as an example. This particular realization is part of an ensemble of photographic PIV measurements made at a Reynolds number $Re_D = 50{,}000$ ($R^+ = 1300$, $U_{CL} = 7.7$ m/s) by Urushihara et al. (1993). Velocity data extends nearly 500 viscous wall units in the streamwise direction (x_1^+) and over 250 wall units in the radial direction (x_2^+). A block of data in the upper left-hand corner of the field has been removed due to severe laser flare from the pipe wall. The PIV photographs were interrogated using 454-μm × 454-μm interrogation spots with 50% overlap, yielding a grid spacing of 227-μm in each direction (4.5 viscous wall units). This high spatial resolution permitted visualization of vortices as small as two Kolmogorov scales ($\eta^+ = 4.56$).

3.1 Galilean Decomposition

In this section, we illustrate the visualization of small-scale vortices by Galilean decomposition. The aforementioned field is shown in Figure 3(a,b,c) with three different

convection velocities removed: $U_{c1} = 0.5\ U_{CL}$, $0.75\ U_{CL}$ and $0.81\ U_{CL}$, respectively. The visible vortices are labeled A-I. Each value of the convection velocity corresponds to a different translational velocity of groups of vortices embedded within the flow. When the convection velocity matches an eddy's translational velocity, it becomes recognizable as a roughly circular pattern of vectors as defined by Kline and Robinson (1989 a, b).

For $U_{c1} = 0.5\ U_{CL}$ (Figure 3(a)), five vortices near the wall ($x_2^+ < 60$) are exposed (A, B, C, D, and E). The vortices in this example lie just above the interface between the buffer and logarithmic regions of the wall layer. In addition, a large region of relatively uniform momentum (darkened portion of the velocity map) is exposed (roughly between $100 < x_1^+ < 300$ and $100 < x_2^+ < 250$).

For $U_{c1} = 0.75\ U_{CL}$ (Figure 3(b)), two more vortices (F, G) are revealed further away from the wall ($50 < x_2^+ < 150$), along with vortex D, which was also seen in the previous case (although its apparent center has moved slightly further away from the wall in this frame). The fact that D is still recognizable as a vortex in this frame of reference indicates that it is not necessary to remove an eddy's exact translational velocity in order to visualize it. This particular value of convection velocity happens to correspond to the frame-averaged streamwise velocity. The Q2 (stress-producing) events induced by these vortices near the wall are also visualized ($0 < x_1^+ < 470$ and $x_2^+ < 70$). An outer region vortex (H) is partially evident in this frame of reference; however, its velocity vector pattern is not completely circular, implying that this is not the most appropriate frame in which to visualize it. Additionally, the uniform momentum zone in the outer region of the field discussed in the previous case is still visible at this convection velocity.

Finally, for $U_{c1} = 0.81\ U_{CL}$ (Figure 3(c)), a new outer region ($x_2^+ > 200$) vortex is visualized (I), along with those already seen in Figure 3(b) (D, F, G, H). It is important to note that vortex H has now become much more circular in this reference frame as compared to the previous one. The uniform momentum zone in the outer region is less visible in this frame of reference, although the Q2 events near the wall are still quite strong. It is evident from this discussion that one must consider a range of convection velocities in order to identify the majority of the turbulent eddies embedded in a velocity field.

3.2 Reynolds Decomposition

As mentioned previously, Reynolds decomposition is the traditional method of decomposing a turbulent velocity field. Reynolds decomposition of our pipe flow example (Figure 4(a)) reveals six vortices (A, B, C, D, E, H), mostly near the wall. Reynolds decomposition tends to reveal more vortices than any single Galilean decomposition because, to a first approximation, the vortices tend to move at the local mean velocity. Therefore, by subtracting the mean velocity profile, $U(x_2^+)$, many more vortices are visualized than by removing a single convection velocity. One of the strengths of Reynolds decomposition is that it does a fair job of revealing the small-scale vortices.

One of the weaknesses of Reynolds decomposition is that it removes large-scale features (mechanisms) that are intimately associated with the mean flow. Thus, comparing Figures 3(a,b,c,d) and 4(a), one sees large regions of relatively uniform momentum in the Galilean decomposition that are not as visible in the Reynolds-decomposed field. In addition, the Q2 events associated with the vortices are less visible in the Reynolds decomposition. These regions provide important clues as to the structure of the logarithmic layer (Meinhart and Adrian 1995).

3.3 LES Decomposition

3.3.1 Homogeneous Filtering

If the small-scale vortices translate with the velocity of the larger-scale vortices in which they are embedded, then the small-scale field obtained by LES decomposition should reveal all of the small-scale eddies in the field. In this study, a homogeneous Gaussian filter was used to compute the filtered field. Figure 4(b) shows the small-scale velocity field for our pipe flow example. It was obtained by subtracting the filtered field from the total velocity field. As expected, the small-scale field reveals eddies from all three of the layers noted in Figure 3, indicating that it is superior to both Reynolds and Galilean decomposition as an eddy visualization tool. Note that the fluctuating field does not provide any insight into regions of constant momentum. However, the filtered field itself should show the large-scale features of the flow, i.e. the uniform momentum zones. In Figure 4(c), regions of near-constant momentum

are evident for $100 < x_1^+ < 375$ and $x_2^+ > 100$. These coincide well with those seen in the Galilean decompositions, especially Figure 3(a).

3.3.2 Inhomogeneous Filtering (Proper Orthogonal Decomposition)

One of the problems with using homogeneous filtering in a turbulent flow field that has statistically inhomogeneous directions is that the character of the filter should change as a function of the inhomogeneous coordinate. That is, in the case of wall-bounded flow, the width of the low-pass filter should grow as a function of the distance from the wall, x_2, to reflect the fact that the turbulent eddies increase in size as one moves away from the wall. This problem can be addressed by using the method of *proper orthogonal decomposition* (POD) to construct low-pass filters that are inhomogeneous in one or more directions. POD provides an optimal set of basis functions for an ensemble of data. It is optimal in the sense that it is the most efficient way of extracting the most-energetic components of an infinite-dimensional process with only a few modes (Holmes et al. 1996).

Consider, for example, time-dependent data on a two-dimensional domain $\boldsymbol{x} = (x_1, x_2)$. In the most general form, the velocity can be expanded as

$$u_i(\boldsymbol{x},t) = \sum_k \sum_n a^{(k,n)}(t)\psi_i^{(k,n)}(\boldsymbol{x}) \tag{6}$$

where ψ_i is an orthogonal basis for the ith component of the velocity and the a's are the time-dependent coefficients of the expansion. The time-dependent coefficients are extracted using the orthogonality of the basis members. This gives

$$a^{(k,n)}(t) = \frac{1}{L_{x_1} L_{x_2}} \int\int u_i(\boldsymbol{x},t)\psi_i^{(k,n)*}(\boldsymbol{x})d\boldsymbol{x} \tag{7}$$

where L_{x_j} is the extent of the domain in the x_j direction and (*) denotes the complex conjugate value.

To illustrate the effectiveness of POD as a filtering tool, we will use photographic PIV measurements made in fully-developed turbulent channel flow at a Reynolds number of 5378 based on the bulk velocity and the half-height of the channel (Liu et al. 1991, 1999). This particular flow allows us to reduce the problem to a two-dimensional one and specialize the form of the basis because the streamwise direction is homogeneous. In this case, we can write ψ_i as

the product of a Fourier basis in the streamwise direction and an optimal, inhomogeneous basis (ϕ_i) in the wall-normal direction as

$$\psi_i^{(k,n)}(x_1, x_2) = \phi_i^{(k,n)}(x_2) e^{i 2\pi k x_1 / L_{x_1}} \tag{8}$$

(Note: $i = \sqrt{-1}$). By doing this, we have converted a 2-D problem into a 1-D POD problem in the inhomogeneous, wall-normal direction.

We can now define the *POD filter*. The total field is separated into a filtered (large-scale) field and a small-scale field

$$\boldsymbol{u} = \overline{\boldsymbol{u}} + \boldsymbol{u}'' \tag{9}$$

where the filtered field is given by

$$\overline{u}_i(x_1, x_2) \equiv \sum_{k=0}^{K} \sum_{n=0}^{N} H^{(k,n)} a^{(k,n)} \psi_i^{(k,n)}(x_1, x_2). \tag{10}$$

Here, $H^{(k,n)}$ is a filter characteristic function that amplifies or attenuates the strength of each mode. If $H^{(k,n)}$ is complex, it also changes the phase of each mode. $H^{(k,n)}$ is completely analogous to the function $H(k, \omega)$ one would apply to a Fourier space representation for a homogeneous signal.

We can write an expression for the filter in physical space in the form of a convolution of the original velocity field and a POD filter kernel, h:

$$\overline{u}_i(x_1', x_2') = \frac{1}{L_{x_1} L_{x_2}} \int\int u_j(x_1', x_2') h_{ij}(x_1, x_2, x_1', x_2') dx_1' dx_2'. \tag{11}$$

The filter kernel is analogous to the impulse response function. It is given by

$$h_{ij} = \sum_{k=0}^{K} \sum_{n=0}^{N} H^{(k,n)} \psi_i^{(k,n)}(x_1, x_2) \psi_j^{(k,n)*}(x_1', x_2'). \tag{12}$$

Figure 5(a) shows the Reynolds-decomposed fluctuations for our fully-developed, turbulent channel flow example. Figure 5(b) illustrates the filtered (large-scale) field obtained when $H^{(k,n)}$ includes the twelve most-energetic modes, i.e. $H^{(k,n)} = 1$ for $k = 0,1,2$ and $n = 1,2,3,4$. These twelve modes contain 48% of the total energy and 75% of the total Reynolds stress,

$<u_1 u_2>$. The small-scale field is shown in Figure 5(c). POD filtering is a very effective scale decomposition in flows with inhomogeneous directions.

3.4 Vortex Identification

As mentioned previously, vorticity analysis is generally used to identify locations of vortices and to calculate vortex statistics (size, strength, etc.). Vorticity, ω, is defined as

$$\omega = \nabla \times \boldsymbol{u} . \tag{13}$$

Unfortunately, vorticity not only identifies vortex cores but also any shearing motions present in the flow. In wall turbulence, strong shear layers populate the near-wall region and tend to mask turbulent eddies in vorticity maps. These shearing motions can render the task of computing reliable vortex statistics virtually impossible.

Several groups have proposed new methods of extracting underlying structure from velocity fields which involve analysis of the local velocity gradient tensor and its corresponding eigenvalues (Chong et al. 1990; Dallman et al. 1991; Zhou et al. 1996, 1999) and the Hessian of pressure (Jeong and Hussain 1995). In three dimensions, the local velocity gradient tensor will have one real eigenvalue (λ_r) and a pair of complex conjugate eigenvalues ($\lambda_{cr} \pm i\lambda_{ci}$) when the discriminant of its characteristic equation is positive. When this is true, the particle trajectories about the eigenvector corresponding to λ_r exhibit a swirling spiral motion (Chong et al. 1990). λ_{ci}^{-1} represents the period required for a particle to swirl once about the λ_r-axis. If the flow is pure shear flow, the particle orbits are infinitely-long ellipses and the orbit period is also infinite, corresponding to $\lambda_{ci} = 0$. Thus, $\lambda_{ci} > 0$ corresponds to shorter, more circular ellipses, i.e. eddies. Zhou et al. (1996, 1999) show that the strength of any local swirling motion is quantified by λ_{ci}, the *swirling strength* of the vortex. Vortex identification based on swirling strength is frame independent, meaning that *a priori* choice of a correct reference frame is not necessary. In addition, it does not reveal regions which have vorticity but are absent of any local swirling motion (i.e., shear layers).

Since PIV fields are usually two-dimensional, the full local velocity gradient tensor cannot be formed. However, an equivalent two-dimensional form of this tensor can be computed in the plane in which the PIV data lies; namely,

$$\underline{\underline{D}}^{2-D} = \begin{bmatrix} \partial u_1 / \partial x_1 & \partial u_1 / \partial x_2 \\ \partial u_2 / \partial x_1 & \partial u_2 / \partial x_2 \end{bmatrix} \tag{14}$$

where (x_1, x_2) and (u_1, u_2) are the streamwise and wall-normal directions and velocities, respectively. In this case, $\underline{\underline{D}}^{2-D}$ will either have two real eigenvalues or a pair of complex conjugate eigenvalues. Therefore, vortices are easily identified by plotting iso-regions of $\lambda_{ci} > 0$.

This analysis was performed on the same pipe flow realization presented earlier. Spatial derivatives were computed using a second-order, central difference scheme. Iso-regions of swirling strength are shown in Figure 6(a). Swirling strength is noted at all locations where a vortex was identified in the various velocity decompositions (labeled A-I). In addition, the swirling strength analysis reveals four additional vortices that were not identified in any of the velocity decompositions. These new vortices are labeled J-M. Figure 6(b) shows vorticity contours and swirling strength iso-lines superimposed on one-another. Although vorticity does identify the eddies fairly well, it is much noisier than the swirling strength, and it also tends to identify local shear layers present in the field. These shortcomings of vorticity make swirling strength more appropriate as a means of identifying eddies.

If one finds the peaks in swirling strength and then performs a *local* Galilean decomposition in the immediate vicinity of the vortex, the swirling motion around these peaks can be confirmed. This is shown in Figure 6(c). Indeed, swirling motion exists around *all* of the regions where significant swirling strength exists. This validates our findings in the velocity decompositions where the Kline and Robinson (1989 a,b) definition was used to identify eddies. Vortices L and M, which were not seen in the velocity decompositions, have a clockwise rotation, while all of the other vortices have a counterclockwise rotation.

3.5 Small-Eddy Decomposition

We can continue the swirling strength analysis one step further and actually use it to separate the small-scale structure from the total field. A 'mean eddy' can be formed by taking the conditional average of the velocity field around the peaks in swirling strength. This can be written as

$$\boldsymbol{u}_V = \langle \boldsymbol{u}(\boldsymbol{x} - \boldsymbol{x}_c) - \boldsymbol{u}(\boldsymbol{x}_c) \mid \boldsymbol{x}_c \rangle \tag{15}$$

where x_c is the center of the vortex as determined from swirling strength. Figure 7 shows the 'mean eddy' found from our single pipe flow realization. The thirteen vortices noted in Figure 6(a) were used in this conditional average. The average diameter of these small-scale vortices is 20 wall units.

Now, the total field can be filtered using this 'mean eddy' as the filter (equation (3)). This is what we refer to as *Small-Eddy Decomposition* (SED). SED provides a true small-scale/large-scale separation because the filter is based upon the small-scale structure embedded in the flow field. Figure 8 shows the small-scale field obtained by SED. Filtering was performed in real space so that the presence of missing vectors could be taken into account. The small-scale field found by SED looks qualitatively similar to the LES-decomposed small-scale field calculated using a Gaussian filter kernel. It clearly isolates vortices A-I, the same vortices seen in the other velocity decompositions.

4 Visualization of Turbulent Stresses

4.1 Reynolds Decomposition

When the total velocity is decomposed using Reynolds averaging, the equation governing the mean velocity (for incompressible flow) is

$$\rho\left(\frac{\partial U_i}{\partial t}+U_j\frac{\partial U_i}{\partial x_j}\right)=-\frac{\partial}{\partial x_j}\left(-p\delta_{ij}-\left\langle u_i'u_j'\right\rangle+\mu\frac{\partial U_i}{\partial x_j}\right) \tag{16}$$

where U_i is the mean and u_i' is the fluctuating portion of the ith component of velocity, ρ is the density of the fluid, and μ is the shear viscosity. The Reynolds (turbulent) stresses (second term on the right-hand side of (16)) are a direct result of the velocity decomposition, and they couple the mean and fluctuating velocity equations. The kinetic energy equations (mean and fluctuating) show that the Reynolds stresses are a source of turbulent kinetic energy and a sink for the kinetic energy of the mean. Therefore, these stresses play a crucial role in understanding the underlying dynamics of turbulence.

4.2 Galilean Decomposition

In other reference frames, turbulent stresses still exist; however, they may not be precisely the same as the Reynolds stresses. In a Galilean frame, the turbulent stresses are the product of the fluctuations obtained by subtracting a constant convection velocity from the total velocity field. The ensemble-averaged Galilean turbulent stresses can be written as

$$\left\langle u_{ci}u_{cj}\right\rangle = \left\langle \left(u_i - U_{Ci}\right)\left(u_j - U_{Cj}\right)\right\rangle . \tag{17}$$

If we express the total velocity in terms of a Reynolds-decomposed field, the Galilean stresses can be related to the original Reynolds stresses as

$$-\left\langle u_{ci}u_{cj}\right\rangle = -\left\langle u_i'u_j'\right\rangle - \left(U_i - U_{Ci}\right)\left(U_j - U_{Cj}\right). \tag{18}$$

From (18) we conclude that, in general, the Galilean turbulent stresses differ from the Reynolds stresses by a potentially large amount, depending on the size of the second term on the right-hand side of (18). However, there are certain classes of flows for which these stresses are identical. *For a statistically-convergent dataset obtained from a canonical wall-bounded turbulent flow (boundary-layer or fully-developed pipe or channel flow), the ensemble-averaged turbulent shear stresses (i.e., $i \neq j$) as seen in a streamwise-translating Galilean frame are identical to the Reynolds stresses since U_2, U_3, U_{c2}, and U_{c3} are all zero.*

The foregoing observations have a number of implications regarding visualization of turbulent stresses. First, consider visualization of the instantaneous, unaveraged Q2 and Q4 turbulent stresses (negative u_1/positive u_2 and positive u_1/negative u_2, respectively), as shown in Figure 9 for our pipe flow example. We choose to focus on the near-wall region because this is where the most intense stress-producing events occur. The patterns of Q2 and Q4 events reveal the elements of the flow that act to sustain the turbulence because they provide energy to the fluctuating field. However, depending on the reference frame one views them in, these events appear differently even though their average may be the same. Figure 9(a) illustrates these stress-producing events for the Reynolds-decomposed field, while Figures 9(b,c,d) illustrate the stress-producing events in three different Galilean frames: $U_{c1} = 0.5\ U_{CL}$, $0.75\ U_{CL}$, and $0.81\ U_{CL}$. Each is different, and therefore physical conclusions drawn from such data will be frame-dependent. The root cause of this result is the fact that the Reynolds stress tensor are not true

stresses created by physical forces, but only momentum transport that has the form of a stress tensor.

A boxed region is highlighted in Figure 9 to illustrate how the instantaneous stresses-producing events can appear quite different in the various reference frames. Vortex F resides just to the right of the boxed region and recall that it was visualized in the second and third Galilean frames (Figure 3(b, c)) and the LES-decomposed field (Figure 4(b)). This vortex has a counterclockwise motion and induces a Q2 event just upstream of it. In the Reynolds-decomposed field (Figure 9(a)), this event does *not* appear. This Q2 event is also *not* visible in the first Galilean frame (Figure 9(b)). However, in Figure 9(c,d), this Q2 *is* visible because we are visualizing the field in the reference frame of the vortex. This particular example illustrates a very important point: *In order to visualize the dynamics induced by a structure embedded in a flow field, one must move in the same frame of reference as the structure.* Finally, for our particular flow, x_1-averaging the Reynolds-decomposed field $u_i'u_j'$ (Figure 9(a)) or the Galilean frames $u_{ci}u_{cj}$ (Figures 9(b,c,d)) will give the correct mean Reynolds stresses. However, we must emphasize that this is only true in certain situations.

Another approach to understanding the underlying dynamics of the small-scale vortices is to evaluate the net fictitious force fields produced by the turbulent stresses. After all, it is actually the net fictitious force (divergence of turbulent stresses) that directly affects the evolution of the turbulence (see eqn. (16)). From (18), the average net fictitious force due to the fluctuations in the Galilean frame is related to the net fictitious force imposed by the Reynolds fluctuations as

$$-\frac{\partial}{\partial x_j}\left\langle u_{ci}u_{cj}\right\rangle = -\frac{\partial}{\partial x_j}\left\langle u_i'u_j'\right\rangle - \left(U_j - U_{Cj}\right)\frac{\partial U_i}{\partial x_j}. \tag{19}$$

Again, in the most general case, the ensemble-averaged net fictitious force in the Galilean frame is different from that observed in the Reynolds frame. However, for canonical wall-bounded flows, the second term on the right-hand side of (19) is zero for $j\neq 1$. For $j=1$, there are two situations of interest. In boundary-layer flows, the second term is roughly zero, although there is some contribution due to the continual growth of the boundary layer downstream. For fully developed pipe and channel flow, the second term is identically zero because the flow is homogeneous in the streamwise direction. *Therefore, for fully developed flow in pipes and*

channels, the net fictitious force imposed by the fluctuations is equivalent in the Reynolds and Galilean frames.

The instantaneous net fictitious force fields are shown in Figure 10(a, b, c, d) for Reynolds decomposition and three Galilean frames. As with the turbulent-stress visualization, we will focus on the near-wall region of the velocity field where the most-intense small-scale vortices reside. The net fictitious force fields as computed for these different decomposition methods appear qualitatively similar, but quantitatively different. The Galilean fields tend to show regions of larger net force compared to the Reynolds-decomposed result. It is important to note, however, that in this particular flow, line-averaging these net fictitious force fields in the streamwise direction will give equivalent profiles as a function of wall-normal direction. In such cases, the Galilean field of stresses can be interpreted simply.

Now let us focus on the insight that net force fields provide on the dynamics and interactions of the small-scale vortices in our pipe flow example. In Figure 10, a region of relatively large net force is boxed for emphasis. This region corresponds to the upstream extent of the Q2 event imposed by vortices E, G, J and K and the downstream end of the Q4 event created by Vortex D (see Figure 6(a)). This interaction creates an enormous net force not only in the negative streamwise direction, but also away from the wall. This produces and sustains the turbulence.

4.3 LES Decomposition

As in the Galilean frame, the turbulent stresses in the LES-decomposed field are not equivalent to the Reynolds stresses. The turbulent stresses in the LES frame can be related to the Reynolds stresses as

$$\left\langle u_i'' u_j'' \right\rangle = \left\langle u_i' u_j' \right\rangle + \left\langle \left(U_i - \overline{u}_i\right)\left(U_j - \overline{u}_j\right) \right\rangle - \left\langle u_i' \overline{u}_j + u_j' \overline{u}_i \right\rangle . \tag{20}$$

The divergence of the LES-decomposed turbulent stresses is

$$\frac{\partial}{\partial x_j}\left\langle u_i'' u_j'' \right\rangle = \frac{\partial}{\partial x_j}\left\langle u_i' u_j' \right\rangle + \left\langle \left(U_j - \overline{u}_j\right) \frac{\partial}{\partial x_j}\left(U_i - \overline{u}_i\right) \right\rangle - \left\langle \frac{\partial u_i'}{\partial x_j}\overline{u}_j + \frac{\partial \overline{u}_i}{\partial x_j} u_j' \right\rangle . \tag{21}$$

Note that, unlike in the Galilean frame, a simple relationship does not exist between the average of the LES-decomposed turbulent stresses and the Reynolds stresses. Figure 9(e) illustrates the

turbulent stress-producing events in the LES-decomposed field. These events are not as strong as those seen in the Reynolds and Galilean decompositions, although the Q2 event in the boxed region looks qualitatively similar to the others.

5 Conclusions

In order to understand the importance of vortex dynamics on the evolution of the large-scale turbulence, one must be able to visualize the vortices and interpret their contribution to the overall flow accordingly. For statistical analysis, Reynolds decomposition is the most appropriate. However, for visualization of vortex structure, other decompositions are shown to be superior. Galilean transformations allow one to not only visualize the core of the small-scale vortices moving at a particular translational velocity, but also the motions these vortices induce (especially near the wall). Despite these advantages, LES decomposition is still the best method for visualizing all of the small-scale vortices in a flow. Analysis based on the local velocity gradient tensor provides a means of extracting the small-scale vortices from the velocity field, including those which are not visible in the velocity decompositions. Swirling strength also allows one to isolate the velocity field in the vicinity of the vortices in order to assess their contribution to the overall dynamics of the flow. Additionally, it can be used to create a 'small-eddy filter' which permits one to separate the small-scale features of the flow from the larger-scale ones.

Visualization of turbulent-stress-producing events is not as straight forward as visualization of vortices. Instantaneous events (stresses and net fictitious force) appear differently depending on the frame of reference used to visualize the flow. However, the averages of these quantities, in the case of Reynolds and Galilean decomposition, are equivalent for certain flows. This is significant because one could choose to use *only* Galilean decomposition and still arrive at the same Reynolds-stress and net-fictitious-force statistics, at least for canonical wall flows.

Acknowledgements

This research was supported by NSF-ATM grant number 95-22662 and NSF-CTS grant number 96-16219. One of the authors (KTC) was supported by an NSF Graduate Fellowship. The

authors gratefully acknowledge C. D. Meinhart for allowing us to use his PIV data as an example in this paper.

References

Chong MS; Perry AE; Cantwell BJ (1990) A general classification of three-dimensional flow fields. Phys Fluids A2: 765-777

Dallman U; Hilgenstock A; Riedelbanh S; Schulte-Werning B; Vollmers H (1991) On the footprints of three-dimensional separated vortex flows around blunt bodies. AGARD CP-494

Gursul I; Lusseyran D; Rockwell D (1990) On interpretation of flow visualization of unsteady shear flows. Exp Fluids 9: 257-266

Hama FR (1962) Streaklines in a perturbed shear flow. Phys Fluids 5: 644-650

Holmes P; Lumley JL; Berkooz G (1996) Turbulence, coherent structures, dynamical systems and symmetry, Cambridge University Press.

Jeong J; Hussain F (1995) On the identification of a vortex. J Fluid Mech 285: 69-94

Jiménez J; Wray AA; Saffman PG; Rogallo RS (1993) The structure of intense vorticity in isotropic turbulence. J Fluid Mech 255: 65–90

Kline SJ; Robinson SK (1989a) Quasi-coherent structures in the turbulent boundary layer. Part I: status report on a community-wide summary of the data. In Near Wall Turbulence. Proceedings of Zaric Memorial Conference (ed. Kline SJ; Afgan NH). pp. 200-217, New York: Hemisphere

Kline SJ; Robinson SK (1989b) Quasi-coherent structures in the turbulent boundary layer. Part II: verification and new information from a numerically simulated flat-plate boundary layer. In Near Wall Turbulence. Proceedings of Zaric Memorial Conference (ed. Kline SJ; Afgan NH). pp. 218-247, New York: Hemisphere

Liu Z-C; Landreth CC; Adrian RJ; Hanratty TJ (1991) High resolution measurement of turbulent structure in a channel with particle image velocimetry. Exp Fluids 10: 301-312

Liu Z-C; Adrian RJ; Hanratty TJ (1999) A study of turbulent channel flow with proper orthogonal decomposition. In preparation

Meinhart CD; Adrian RJ (1995) On the existence of uniform momentum zones in a turbulent boundary layer. Phys Fluids 7: 694-696

Michalke A (1964) On the inviscid instability of the hyperbolic-tangent velocity profile. J Fluid Mech 19: 543-556

Urushihara T; Meinhart CD; Adrian RJ (1993) Investigation of the logarithmic layer in pipe flow using particle image velocimetry. In Near-Wall Turbulent Flows (ed. So RMC; Speziale CG; Launder BE). pp. 433-446, Leiden: Elsevier Science Publishers

Zhou J; Adrian RJ; Balachandar S (1996) Autogeneration of near-wall vortical structures in channel flow. Phys. Fluids 8: 288-290

Zhou J; Adrian RJ; Balachandar S; Kendall TM (1999) Mechanisms for generating coherent packets of hairpin vortices in channel flow. J Fluid Mech 387: 353-9

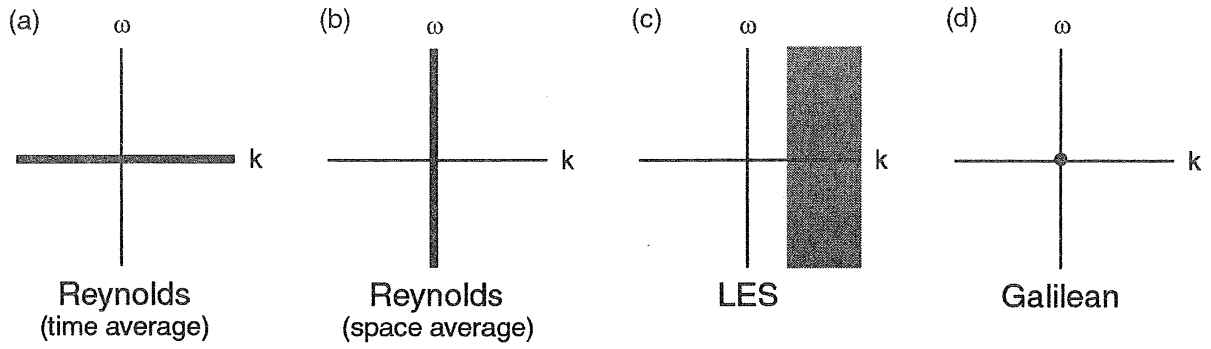

Figure 1. Illustration of various scale decompositions in wave space. (a) Reynolds (time average); (b) Reynolds (space average); (c) LES; (d) Galilean.

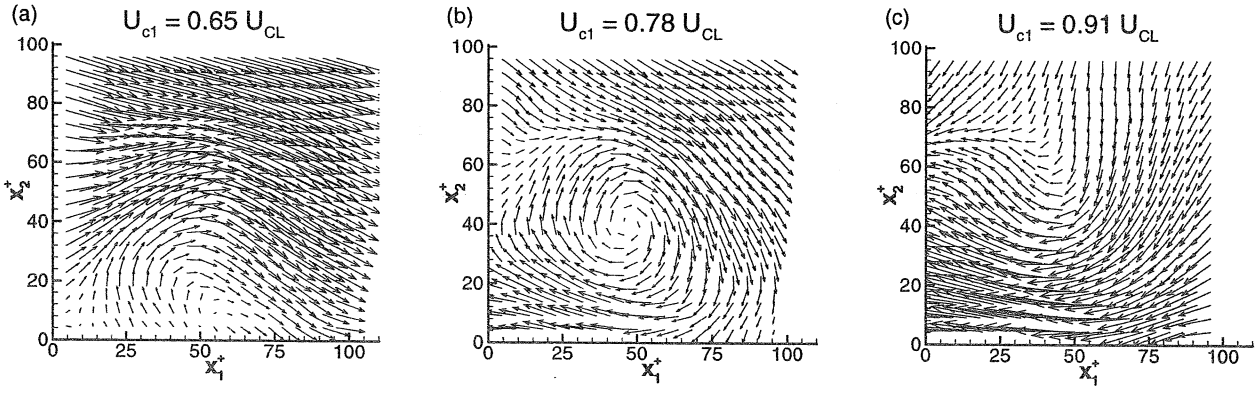

Figure 2. Visualization of an isolated turbulent eddy by Galilean decomposition for three different convection velocities: (a) $U_{c1} = 0.65\ U_{CL}$; (b) $U_{c1} = 0.78\ U_{CL}$; (c) $U_{c1} = 0.91\ U_{CL}$. $U_{c1} = 0.78\ U_{CL}$ is the 'correct' convection velocity based upon the Kline and Robinson (1989 a, b) definition.

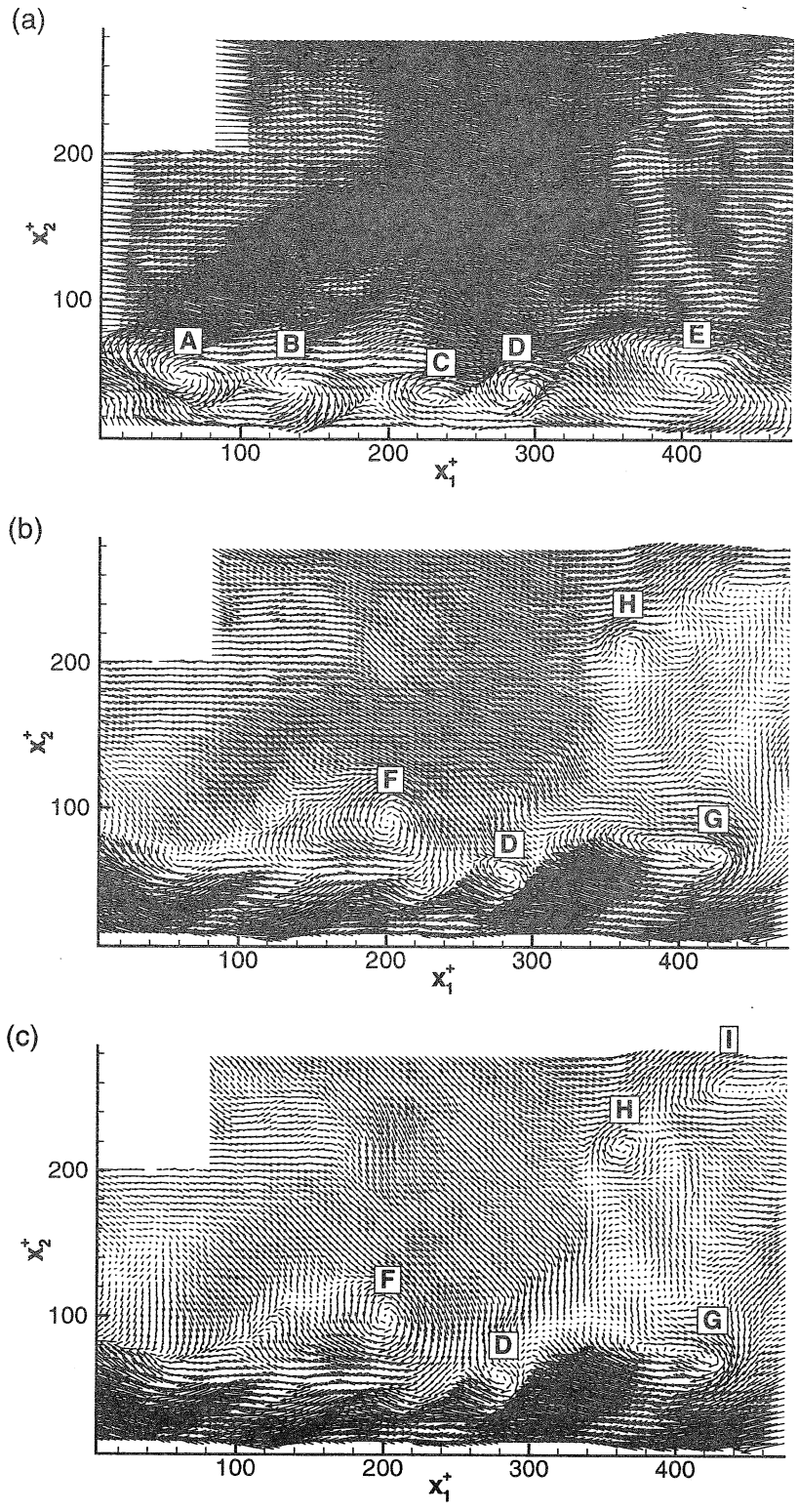

Figure 3. Fluctuating vector fields in pipe flow found by Galilean decomposition. (a) $U_{cl} = 0.5\ U_{CL}$; (b) $U_{cl} = 0.75\ U_{CL}$; (c) $U_{cl} = 0.81\ U_{CL}$. The small-scale vortices are labeled A-I.

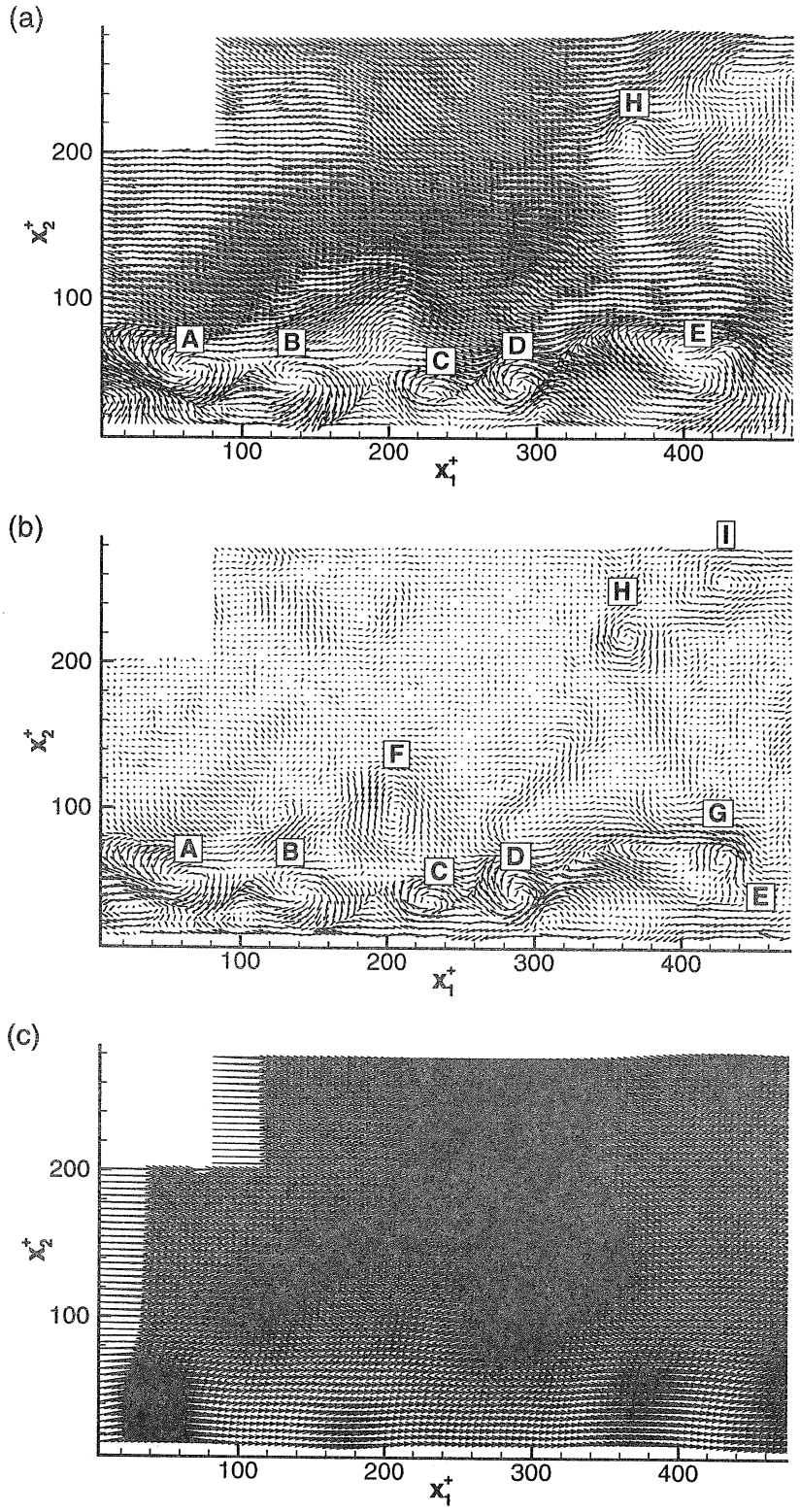

Figure 4. Pipe flow velocity fields illustrating (a) Reynolds-decomposed fluctuations; (b) LES-decomposed fluctuations; (c) LES low-pass filtered field.

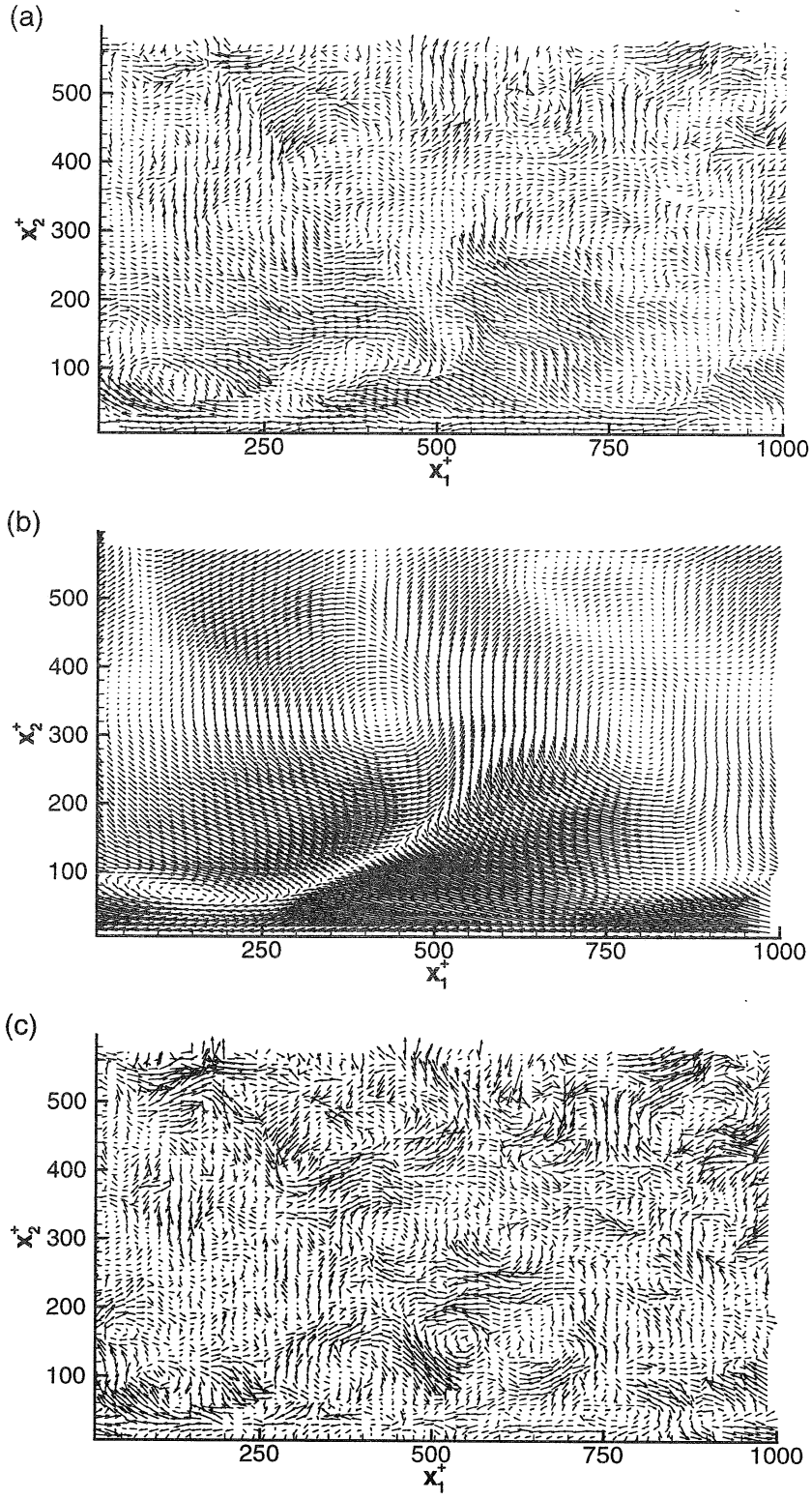

Figure 5. POD of fully developed turbulent channel flow. (a) small-scale field obtained by Reynolds decomposition; (b) large-scale POD field (k = 0,1,2 and n = 1,2,3,4) ; (c) small-scale POD field.

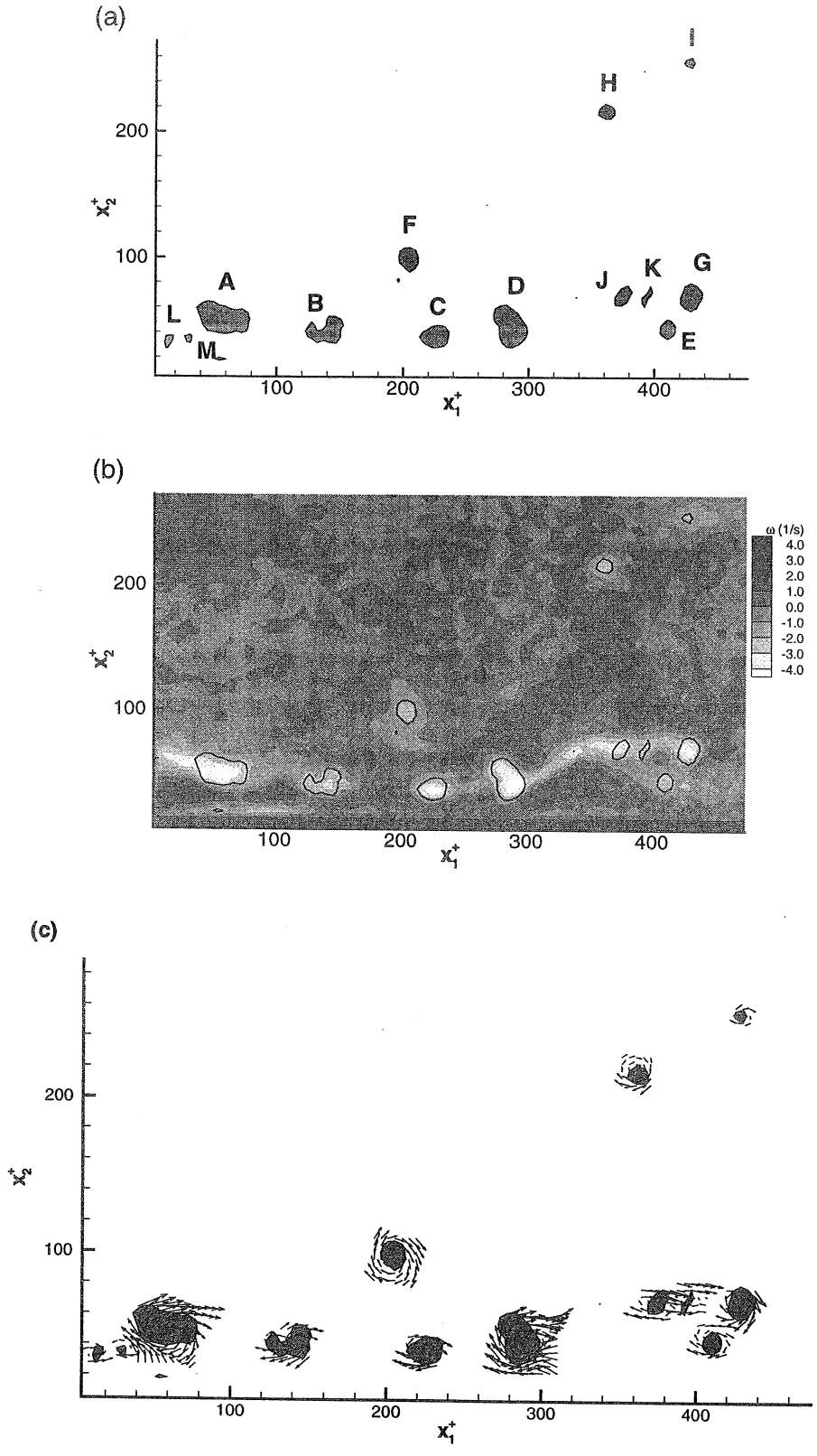

Figure 6. (a) Swirling strength contours and (b) vorticity (gray-scale) and swirling strength (line) contours for pipe flow. (c) Velocity field (in reference frame of the vortex) around peaks in swirling strength.

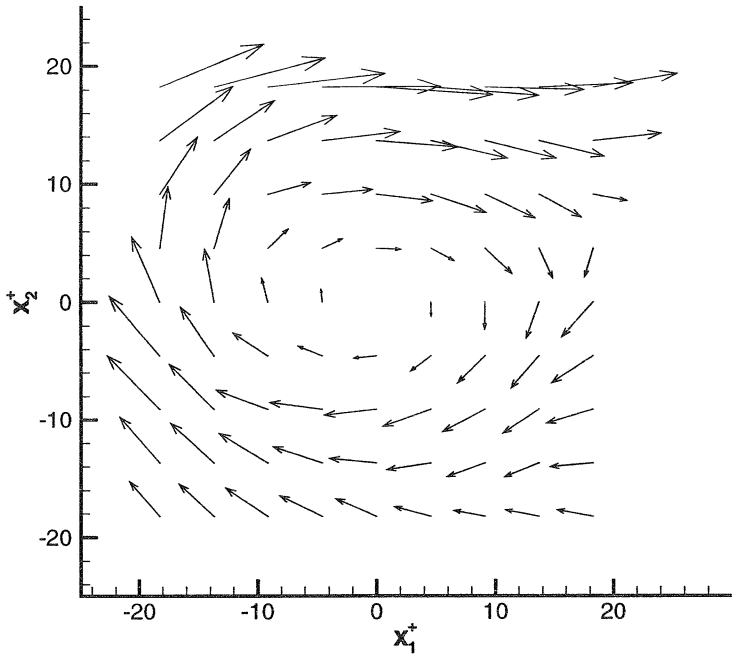

Figure 7. 'Mean eddy' found by conditional averaging velocity field based on peaks in swirling strength.

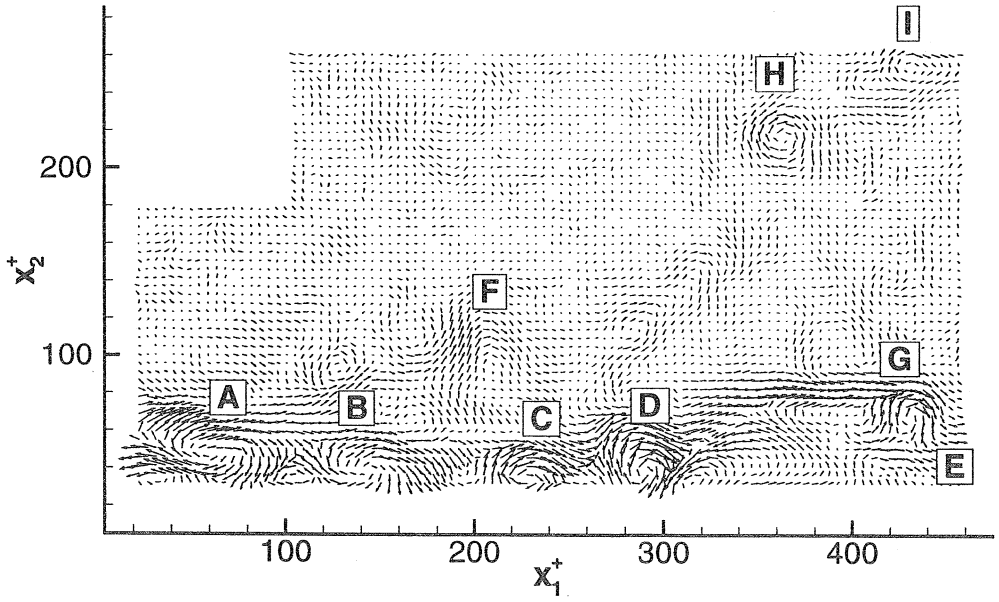

Figure 8. Small-scale velocity field obtained by SED using the 'mean eddy' shown in Figure 7 as the filter.

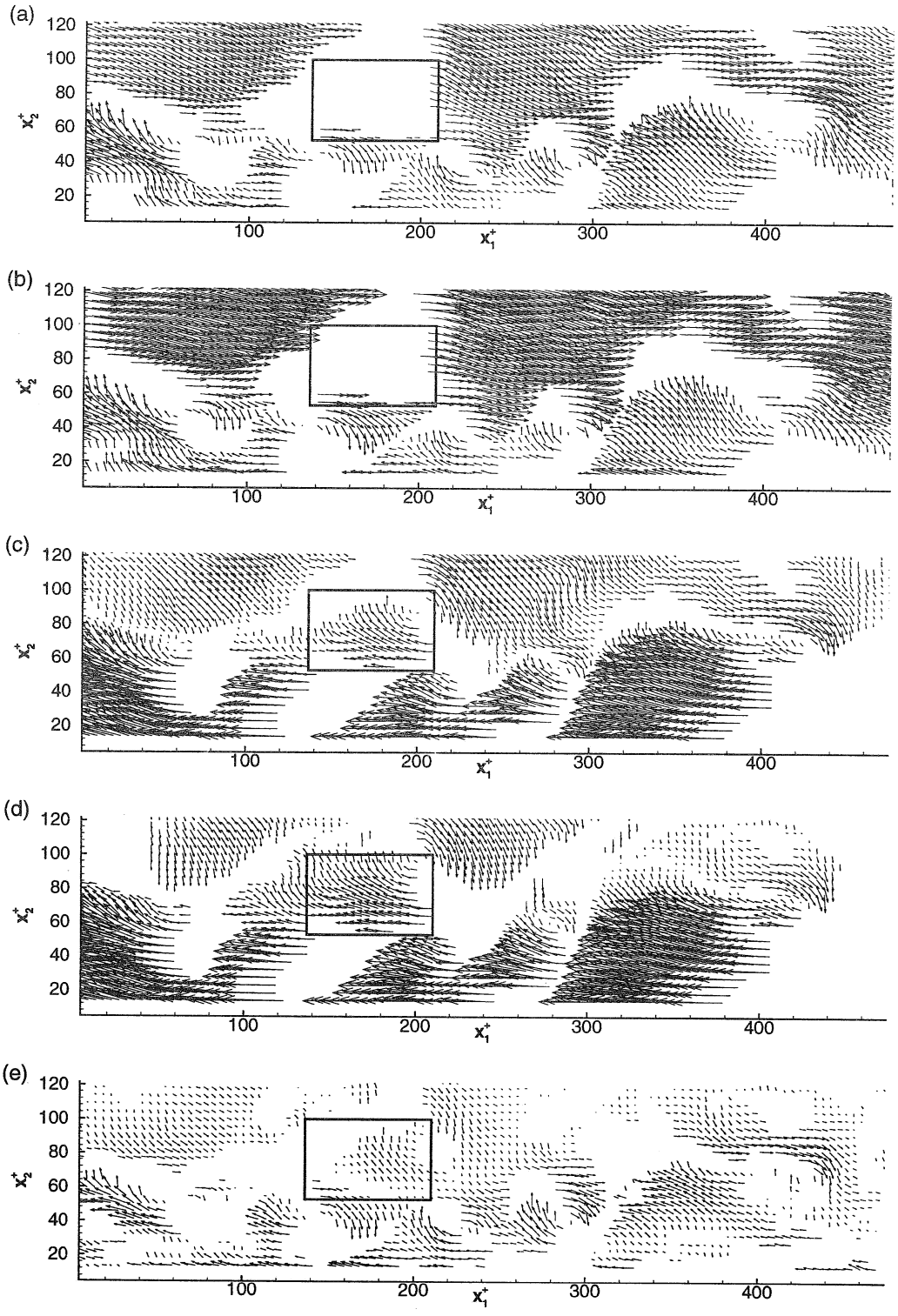

Figure 9. Visualization of Q2 and Q4 events near the wall in pipe flow for five different decompositions. (a) Reynolds decomposition; (b) Galilean $U_{cl} = 0.5\ U_{CL}$; (c) Galilean $U_{cl} = 0.75\ U_{CL}$; (d) Galilean $U_{cl} = 0.81\ U_{CL}$; (e) LES decomposition.

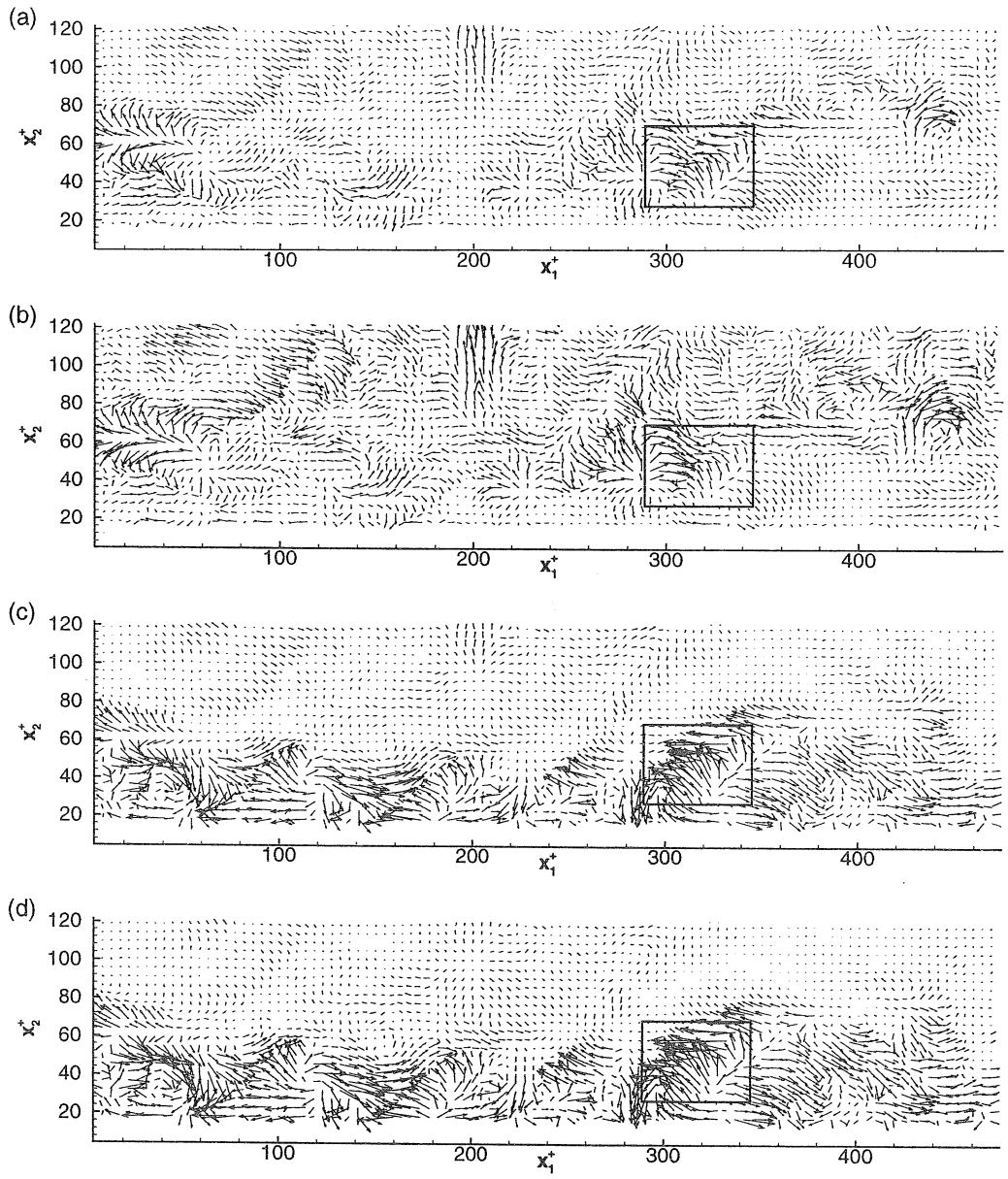

Figure 10. Visualization of net- fictitious-force imposed by the velocity fluctuations near the wall in pipe flow for Reynolds and Galilean decompositions. (a) Reynolds decomposition; (b) Galilean $U_{cl} = 0.5\ U_{CL}$; (c) Galilean $U_{cl} = 0.75\ U_{CL}$; (d) Galilean $U_{cl} = 0.81\ U_{CL}$

List of Recent TAM Reports

No.	Authors	Title	Date
820	Short, M., and D. S. Stewart	Low-frequency two-dimensional linear instability of plane detonation—*Journal of Fluid Mechanics* **340**, 249–295 (1997)	Mar. 1996
821	Casagranda, A., and P. Sofronis	On the scaling laws for the consolidation of nanocrystalline powder compacts—Proceedings of the *IUTAM Symposium on the Mechanics of Granular and Porous Materials*, N. A. Fleck and A. C. F. Cocks, eds. The Netherlands: Kluwer Academic Publishers, 105–116 (1997)	Apr. 1996
822	Xu, S., and D. S. Stewart	Deflagration-to-detonation transition in porous energetic materials: A comparative model study—*Journal of Engineering Mathematics* **31**, 143–172 (1997)	Apr. 1996
823	Weaver, R. L.	Mean and mean-square responses of a prototypical master/fuzzy structure—*Journal of the Acoustical Society of America* **101**, 1441–1449 (1997)	Apr. 1996
824	Fried, E.	Correspondence between a phase-field theory and a sharp-interface theory for crystal growth—*Continuum Mechanics and Thermodynamics* **9**, 33–60 (1997)	Apr. 1996
825	Students in TAM 293–294	Thirty-third student symposium on engineering mechanics, J. W. Phillips, coordinator: Selected senior projects by W. J. Fortino II, A. A. Mordock, and M. R. Sawicki	May 1996
826	Riahi, D. N.	Effects of roughness on nonlinear stationary vortices in rotating disk flows—*Mathematical and Computer Modeling* **25**, 71–82 (1997)	June 1996
827	Riahi, D. N.	Nonlinear instabilities of shear flows over rough walls, *Far East Journal of Applied Mathematics*, in press (1998)	June 1996
828	Weaver, R. L.	Multiple scattering theory for a plate with sprung masses, mean responses—*Journal of the Acoustical Society of America* **101**, 3466–3414 (1997)	July 1996
829	Moser, R. D., M. M. Rogers, and D. W. Ewing	Self-similarity of time-evolving plane wakes *Journal of Fluid Mechanics* **367**, 255–289 (1998)	July 1996
830	Lufrano, J. M., and P. Sofronis	Enhanced hydrogen concentrations ahead of rounded notches and cracks: Competition between plastic strain and hydrostatic stress—*Acta Materialia* **46**, 1519–1526 (1998)	July 1996
831	Riahi, D. N.	Effects of surface corrugation on primary instability modes in wall-bounded shear flows	Aug. 1996
832	Bechel, V. T., and N. R. Sottos	Application of debond length measurements to examine the mechanics of fiber pushout, *Journal of Mechanics and Physics of Solids* **46**, 1675–1697 (1998)	Aug. 1996
833	Riahi, D. N.	Effect of centrifugal and Coriolis forces on chimney convection during alloy solidification—*Journal of Crystal Growth* **179** , 287–296 (1997)	Sept. 1996
834	Cermelli, P., and E. Fried	The influence of inertia on configurational forces in a deformable solid—*Proceedings of the Royal Society of London A* **453**, 1915–1927 (1997)	Oct. 1996
835	Riahi, D. N.	On the stability of shear flows with combined temporal and spatial imperfections	Oct. 1996
836	Carranza, F. L., B. Fang, and R. B. Haber	An adaptive space–time finite element model for oxidation-driven fracture, *Computer Methods in Applied Mechanics and Engineering*, in press (1997)	Nov. 1996
837	Carranza, F. L., B. Fang, and R. B. Haber	A moving cohesive interface model for fracture in creeping materials, *Computational Mechanics* **19**, 517–521 (1997)	Nov. 1996
838	Balachandar, S., R. Mittal, and F. M. Najjar	Properties of the mean wake recirculation region in two-dimensional bluff body wakes—*Journal of Fluid Mechanics*, in press (1997)	Dec. 1996
839	Ti, B. W., W. D. O'Brien, Jr., and J. G. Harris	Measurements of coupled Rayleigh wave propagation in an elastic plate—*Journal of the Acoustical Society of America* **102**, 1528–1531	Dec. 1996

List of Recent TAM Reports (cont'd)

No.	Authors	Title	Date
840	Phillips, W. R. C.	On finite-amplitude rotational waves in viscous shear flows—*Studies in Applied Mathematics* **100**, in press (1998)	Jan. 1997
841	Riahi, D. N.	Direct resonance analysis and modeling for a turbulent boundary layer over a corrugated surface—*Acta Mechanica*, in press (1998)	Jan. 1997
842	Liu, Z.-C., R. J. Adrian, C. D. Meinhart, and W. Lai	Structure of a turbulent boundary layer using a stereoscopic, large format video-PIV—*Developments in Laser Techniques and Fluid Mechanics*, 259–273 (1997)	Jan. 1997
843	Fang, B., F. L. Carranza, and R. B. Haber	An adaptive discontinuous Galerkin method for viscoplastic analysis—*Computer Methods in Applied Mechanics and Engineering* **150**, 191–198 (1997)	Jan. 1997
844	Xu, S., T. D. Aslam, and D. S. Stewart	High-resolution numerical simulation of ideal and non-ideal compressible reacting flows with embedded internal boundaries—*Combustion Theory and Modeling* **1**, 113–142 (1997)	Jan. 1997
845	Zhou, J., C. D. Meinhart, S. Balachandar, and R. J. Adrian	Formation of coherent hairpin packets in wall turbulence—In *Self-Sustaining Mechanisms in Wall Turbulence*, R. L. Panton, ed. Southampton, UK: Computational Mechanics Publications, 109–134 (1997)	Feb. 1997
846	Lufrano, J. M., P. Sofronis, and H. K. Birnbaum	Elastoplastically accommodated hydride formation and embrittlement—*Journal of Mechanics and Physics of Solids*, in press (1998)	Feb. 1997
847	Keane, R. D., N. Fujisawa, and R. J. Adrian	Unsteady non-penetrative thermal convection from non-uniform surfaces—In *Geophysical and Astrophysical Convection*, R. Kerr, ed. (1997)	Feb. 1997
848	Aref, H., and M. Brøns	On stagnation points and streamline topology in vortex flows—*Journal of Fluid Mechanics* **370**, 1–27 (1998)	Mar. 1997
849	Asghar, S., T. Hayat, and J. G. Harris	Diffraction by a slit in an infinite porous barrier—*Wave Motion*, in press (1998)	Mar. 1997
850	Shawki, T. G., H. Aref, and J. W. Phillips	Mechanics on the Web—Proceedings of the International Conference on Engineering Education (Aug. 1997, Chicago)	Apr. 1997
851	Stewart, D. S., and J. Yao	The normal detonation shock velocity–curvature relationship for materials with non-ideal equation of state and multiple turning points—*Combustion* **113**, 224–235 (1998)	Apr. 1997
852	Fried, E., A. Q. Shen, and S. T. Thoroddsen	Wave patterns in a thin layer of sand within a rotating horizontal cylinder—*Physics of Fluids* **10**, 10–12 (1998)	Apr. 1997
853	Boyland, P. L., H. Aref, and M. A. Stremler	Topological fluid mechanics of stirring—*Bulletin of the American Physical Society* **41**, 1683 (1996)	Apr. 1997
854	Parker, S. J., and S. Balachandar	Viscous and inviscid instabilities of flow along a streamwise corner—*Bulletin of the American Physical Society* **42**, 2155 (1997)	May 1997
855	Soloff, S. M., R. J. Adrian, and Z.-C. Liu	Distortion compensation for generalized stereoscopic particle image velocimetry—*Measurement Science and Technology* **8**, 1–14 (1997)	May 1997
856	Zhou, Z., R. J. Adrian, S. Balachandar, and T. M. Kendall	Mechanisms for generating coherent packets of hairpin vortices in near-wall turbulence—*Bulletin of the American Physical Society* **42**, 2243 (1997)	June 1997
857	Neishtadt, A. I., D. L. Vainshtein, and A. A. Vasiliev	Chaotic advection in a cubic stokes flow—*Physica D* **111**, 227 (1997).	June 1997
858	Weaver, R. L.	Ultrasonics in an aluminum foam—*Ultrasonics* **36**, 435–442 (1998)	July 1997
859	Riahi, D. N.	High gravity convection in a mushy layer during alloy solidification—In *Nonlinear Instability, Chaos and Turbulence*, D. N. Riahi and L. Debnath, eds., in press (1998)	July 1997
860	Najjar, F. M., and S. Balachandar	Low-frequency unsteadiness in the wake of a normal plate, *Bulletin of the American Physical Society* **42**, 2212 (1997)	Aug. 1997
861	Short, M.	A parabolic linear evolution equation for cellular detonation instability—*Combustion Theory and Modeling* **1**, 313–346 (1997)	Aug. 1997

List of Recent TAM Reports (cont'd)

No.	Authors	Title	Date
862	Short, M., and D. S. Stewart	Cellular detonation stability, I: A normal-mode linear analysis—*Journal of Fluid Mechanics* **368**, 229–262 (1998)	Sept. 1997
863	Carranza, F. L., and R. B. Haber	A numerical study of intergranular fracture and oxygen embrittlement in an elastic–viscoplastic solid—*Journal of the Mechanics and Physics of Solids*, in press (1997)	Oct. 1997
864	Sakakibara, J., and R. J. Adrian	Whole-field measurement of temperature in water using two-color laser-induced fluorescence—*Experiments in Fluids* **26**, 7–15 (1999)	Oct. 1997
865	Riahi, D. N.	Effect of surface corrugation on convection in a three-dimensional finite box of fluid-saturated porous material	Oct. 1997
866	Baker, C. F., and D. N. Riahi	Three-dimensional flow instabilities during alloy solidification	Oct. 1997
867	Fried, E.	Introduction (only) to *The Physical and Mathematical Foundations of the Continuum Theory of Evolving Phase Interfaces* (book containing 14 seminal papers dedicated to Morton E. Gurtin), Berlin: Springer-Verlag, in press (1998)	Oct. 1997
868	Folguera, A., and J. G. Harris	Coupled Rayleigh surface waves in a slowly varying elastic waveguide—*Proceedings of the Royal Society of London*, in press (1998)	Oct. 1997
869	Stewart, D. S.	Detonation shock dynamics: Application for precision cutting of metal with detonation waves	Oct. 1997
870	Shrotriya, P., and N. R. Sottos	Creep and relaxation behavior of woven glass/epoxy substrates for multilayer circuit board applications—*Polymer Composites* **19**, 567–578 (1998)	Nov. 1997
871	Riahi, D. N.	Boundary wave–vortex interaction in channel flow at high Reynolds numbers, *Fluid Dynamics Research*, in press (1998)	Nov. 1997
872	George, W. K., L. Castillo, and M. Wosnik	A theory for turbulent pipe and channel flows—paper presented at *Disquisitiones Mechanicae* (Urbana, Ill., October 1996)	Nov. 1997
873	Aslam, T. D., and D. S. Stewart	Detonation shock dynamics and comparisons with direct numerical simulation—*Combustion Theory and Modeling*, in press (1999)	Dec. 1997
874	Short, M., and A. K. Kapila	Blow-up in semilinear parabolic equations with weak diffusion	Dec. 1997
875	Riahi, D. N.	Analysis and modeling for a turbulent convective plume—*Mathematical and Computer Modeling* **28**, 57–63 (1998)	Jan. 1998
876	Stremler, M. A., and H. Aref	Motion of three point vortices in a periodic parallelogram—*Journal of Fluid Mechanics*, in press (1999)	Feb. 1998
877	Dey, N., K. J. Hsia, and D. F. Socie	On the stress dependence of high-temperature static fatigue life of ceramics	Feb. 1998
878	Brown, E. N., and N. R. Sottos	Thermoelastic properties of plain weave composites for multilayer circuit board applications	Feb. 1998
879	Riahi, D. N.	On the effect of a corrugated boundary on convective motion	Feb. 1998
880	Riahi, D. N.	On a turbulent boundary layer flow over a moving wavy wall	Mar. 1998
881	Riahi, D. N.	Vortex formation and stability analysis for shear flows over combined spatially and temporally structured walls	June 1998
882	Short, M., and D. S. Stewart	The multi-dimensional stability of weak heat release detonations	June 1998
883	Fried, E., and M. E. Gurtin	Coherent solid-state phase transitions with atomic diffusion: A thermomechanical treatment—*Journal of Statistical Physics*, in press (1999)	June 1998
884	Langford, J. A., and R. D. Moser	Optimal large-eddy simulation formulations for isotropic turbulence	July 1998
885	Riahi, D. N.	Boundary-layer theory of magnetohydrodynamic turbulent convection—*Proceedings of the Indian National Academy (Physical Science)*, in press (1999)	Aug. 1998
886	Riahi, D. N.	Nonlinear thermal instability in spherical shells—in *Nonlinear Instability, Chaos and Turbulence* **2**, in press (1999)	Aug. 1998

List of Recent TAM Reports (cont'd)

No.	*Authors*	*Title*	*Date*
887	Riahi, D. N.	Effects of rotation on fully non-axisymmetric chimney convection during alloy solidification	Sept. 1998
888	Fried, E., and S. Sellers	The Debye theory of rotary diffusion	Sept. 1998
889	Short, M., A. K. Kapila, and J. J. Quirk	The hydrodynamic mechanisms of pulsating detonation wave instability	Sept. 1998
890	Stewart, D. S.	The shock dynamics of multidimensional condensed and gas phase detonations—Proceedings of the 27th International Symposium on Combustion (Boulder, Colo.)	Sept. 1998
891	Kim, K. C., and R. J. Adrian	Very large-scale motion in the outer layer	Oct. 1998
892	Fujisawa, N., and R. J. Adrian	Three-dimensional temperature measurement in turbulent thermal convection by extended range scanning liquid crystal thermometry	Oct. 1998
893	Shen, A. Q., E. Fried, and S. T. Thoroddsen	Is segregation-by-particle-type a generic mechanism underlying finger formation at fronts of flowing granular media?—*Particulate Science and Technology*, in press (1999)	Oct. 1998
894	Shen, A. Q.	Mathematical and analog modeling of lava dome growth	Oct. 1998
895	Buckmaster, J. D., and M. Short	Cellular instabilities, sub-limit structures, and edge-flames in premixed counterflows	Oct. 1998
896	Harris, J. G.	*Elastic waves*—Part of a book to be published by Cambridge University Press	Dec. 1998
897	Paris, A. J., and G. A. Costello	Cord composite cylindrical shells	Dec. 1998
898	Students in TAM 293–294	Thirty-fourth student symposium on engineering mechanics (May 1997), J. W. Phillips, coordinator: Selected senior projects by M. R. Bracki, A. K. Davis, J. A. (Myers) Hommema, and P. D. Pattillo	Dec. 1998
899	Taha, A., and P. Sofronis	A micromechanics approach to the study of hydrogen transport and embrittlement	Jan. 1999
900	Ferney, B. D., and K. J. Hsia	The influence of multiple slip systems on the brittle–ductile transition in silicon	Feb. 1999
901	Fried, E., and A. Q. Shen	Supplemental relations at a phase interface across which the velocity and temperature jump	Mar. 1999
902	Paris, A. J., and G. A. Costello	Cord composite cylindrical shells: Multiple layers of cords at various angles to the shell axis	Apr. 1999
903	Ferney, B. D., M. R. DeVary, K. J. Hsia, and A. Needleman	Oscillatory crack growth in glass	Apr. 1999
904	Fried, E., and S. Sellers	Microforces and the theory of solute transport	Apr. 1999
905	Balachandar, S., J. D. Buckmaster, and M. Short	The generation of axial vorticity in solid-propellant rocket-motor flows	May 1999
906	Aref, H., and D. L. Vainchtein	The equation of state of a foam	May 1999
907	Subramanian, S. J., and P. Sofronis	Modeling of the interaction between densification mechanisms in powder compaction	May 1999
908	Aref, H., and M. A. Stremler	Four-vortex motion with zero total circulation and impulse	May 1999
909	Adrian, R. J., K. T. Christensen, and Z.-C. Liu	On the analysis and interpretation of turbulent velocity fields	May 1999